Biosensors and Bioelectronics 74 (2015) 347–352

Contents lists available at ScienceDirect

Biosensors and Bioelectronics

journal homepage: www.elsevier.com/locate/bios

Novel phenol biosensor based on laccase immobilized on reduced graphene oxide supported palladium–copper alloyed nanocages

Li-Ping Mei, Jiu-Ju Feng, Liang Wu, Jia-Ying Zhou, Jian-Rong Chen, Ai-Jun Wang *

College of Geography and Environmental Science, College of Chemistry and Life Science, Zhejiang Normal University, Jinhua 321004, China

ARTICLE INFO

Article history:
Received 15 April 2015
Received in revised form
15 June 2015
Accepted 25 June 2015
Available online 30 June 2015

Keywords:
Alloyed nanocages
Reduced graphene oxide
Laccase
Biosensor
Catechol

ABSTRACT

Developing new nanomaterials is of key importance to improve the analytical performances of electrochemical biosensors. In this work, palladium–copper alloyed nanocages supported on reduced graphene oxide (RGO–PdCu NCs) were facilely prepared by a simple one-pot solvothermal method. A novel phenol biosensor based on laccase has been constructed for rapid detection of catachol, using RGO–PdCu NCs as electrode material. The as-developed phenol biosensor greatly enhanced the electrochemical signals for catechol. Under the optimal conditions, the biosensor has two linear ranges from 0.005 to 1.155 mM and 1.655 to 5.155 mM for catachol detection at 0.6 V, the sensitivity of 12.65 μA mM^{-1} and 5.51 μA mM^{-1}, respectively. This biosensor showed high selectivity, low detection limit, good reproducibility, and high anti-interference ability.

1. Introduction

Phenol compounds have attracted great interest as a kind of widespread contaminant compounds for their toxicity and possible accumulation in the environment (Skladal et al. 2002; Stoytcheva et al., 2015). As one of phenol compounds, catechol originated mainly from a variety of chemicals and pesticides, possesses a serious threat to human and environmental health (Li et al., 2014a, 2014b, 2014c; Wolfrum et al., 2008; Zhou et al., 2014). Therefore, it is essential to develop a facile analytical method for trace detection of catechol.

For accurate determination of catechol in biological media, a variety of methods have been developed, such as high-performance liquid chromatography (Marrubini et al., 2005), spectrophotometer (Naczk and Shahidi, 2004), enzyme immunoassays (Barek et al., 1994), and electrochemical approaches (Wightman, 2006). However, their practical applications are seriously restricted because of the high cost, complicated procedures, and time-consuming in the above methods, albeit with their high sensitivity and low detection limit. Hence, many efforts are devoted to the development of simple and effective methods for catechol determination.

As a group of blue multi-copper oxidases, laccase (Lac) can catalyze the oxidation of phenols, coupled with the reduction of O_2 to H_2O (Giardina et al., 2010). As a consequence, numerous phenol biosensors based on Lac have been fabricated for the determination of phenols (Brondani et al., 2013; Tan et al., 2009; Zhou et al., 2013), because they have the advantages of high selectivity, convenience, reliability, and high sensitivity (Fu et al., 2014; Portaccio et al., 2010).

To further improve the performance of biosensors, bimetallic nanomaterials have been employed as the electrode modifier in biosensors, attributing to their enlarged specific surface area, superior conductivity, and biocompatibility (Gao et al., 2011). Particularly, Pd-based nanocomposites have attracted great attention as its high conductivity, large active surface area, and good catalytic activity for use in biosensor (Niu et al., 2012; Yang et al., 2015). For example, Zhao et al. synthesized palladium–gold nanopariticles (Pd–Au NPs) for the construction of a novel electrochemical immunosensor to detect alpha fetoprotein, in which Pd–Au NPs was used for signal amplification (Zhao et al., 2013).

However, bimetallic nanomaterials tend to agglomerate during the repeated use in catalysis (Lee et al., 2014). This issue can be efficiently overcome by introducing graphene oxide (GO) as a supporting material for its strong adhesion to bimetallic catalysts (Li et al., 2014a, 2014b, 2014c). Additionally, its high electrical conductivity, large surface area, flexibility and chemical inertness render the supported bimetallic catalysts widely practical applications in catalysis (Wang et al., 2015).

Herein, well-defined reduced graphene oxide supported Pd–Cu alloyed nanocages (RGO–PdCu NCs) were used as an enzyme immobilization platform, which was explored for the construction of

* Corresponding author. Fax: +86 579 82282269.
E-mail address: ajwang@zjnu.cn (A.-J. Wang).

http://dx.doi.org/10.1016/j.bios.2015.06.060
0956-5663/

a novel phenol biosensor for the determination of catechol as a model system.

2. Experimental section

2.1. Chemicals and materials

Palladium acetylacetonate ($Pd(acac)_2$), copper acetylacetonate ($Cu(acac)_2$), N, N-dimethylformamide (DMF), n-butylamine, graphite powder, and cetyltrimethylammonium chloride (CTAC) were purchased from Shanghai Aladdin Chemical Reagent Company (Shanghai, China. Laccase (Lac)) and catechol were obtained from Sigma-Aldrich Chemical Co., Ltd. (St. Louis, MO, USA). All the other chemicals were analytical grade and used without further purification. All of the aqueous solutions were prepared with twice-distilled water throughout the whole experiments.

2.2. Characterization

The morphology and composition of the products were examined by transmission electron microscopy (TEM), high-resolution transmission electron microscopy (HRTEM), energy-dispersive X-ray spectroscopy (EDS), and high-angle annular dark-field scanning transmission electron microscopy (HAADF-STEM) recording on a JEM-2100F transmission electron microscope coupled with an energy-dispersive X-ray spectrometer (Oxford-1NCA). The crystal structures were characterized by X-ray diffraction (XRD) on a Rigaku Dmax-2000 diffractometer (Bruker Co., Germany) with Cu Kα radiation source ($\lambda = 0.15418$ nm). The surface properties were determined by X-ray photoelectron spectroscopy (XPS) measurements on a K-Alpha XPS spectrometer (ThermoFisher, E. Grinstead, UK) with Al Kα X-ray radiation (1486.6 eV) for excitation. Raman spectra were acquired on a Renishaw Raman system model 1000 spectrometer equipped with an excitation wavelength of 633 nm. Thermo gravimetric analysis (TGA) was conducted with a simultaneous thermo-gravimetric analyzer (NETZSCH STA 449 C). The samples were heated in air from room temperature to 800 °C with a heat rate of 10 °C min^{-1}.

2.3. Preparation of RGO–PdCu NCs

Prior to use, GO was prepared from natural graphite powder by a modified Hummers' method (Hummers Jr. and Offeman, 1958; Sahu et al., 2013). For typical synthesis of RGO–PdCu NCs, 3.1 mg of $Pd(acac)_2$ and 7.8 mg of $Cu(acac)_2$ were dissolved into 3 mL of DMF under vigorous stirring. Next, 5 mL of GO (1 mg mL^{-1}), 10 mL of CTAC (0.01 M in DMF), and 1.5 mL of n-butylamine were successively mixed with the above solution and continually stirred for 15 min. The resulting homogeneous suspension was transferred into a 25 mL Teflon-lined stainless-steel autoclave, sealed the vessel and heated at 150 °C for 10 h, followed by cooling to room temperature in air. The final products were collected by centrifugation and thoroughly washed with ethanol and water to remove the impurities, and dried at 60 °C in vacuum for further characterization.

In control experiments, RGO–Pd NPs and RGO–Cu NPs were fabricated in a similar way. Besides, pure RGO were obtained by reducing GO with $NaBH_4$, while the other experimental conditions were kept unchanged.

2.4. Electrochemical measurements

Cyclic voltammetry, electrochemical impedance spectroscopy (EIS), and chronoamperometry measurements were all carried out on a CHI660E electrochemical workstation (Chenhua Instruments Co., Shanghai, China) with a conventional three-electrode system: a bare or modified glassy carbon electrode (GCE, $\varphi = 3.0$ mm) was employed as the working electrode, a platinum foil as the counter electrode, and a saturated calomel electrode (SCE, saturated KCl) as the reference electrode, respectively.

For typical construction of Lac/RGO–PdCu NCs/GCE, 4.0 mg of Lac was dispersed into 4 mL of acetate buffer solution under stirring. After 15 min, 4.0 mg of RGO–PdCu NCs was put into the above Lac suspension, and then the mixture was constantly stirred for 24 h in ice-bath to get a homogenous suspension. Next, 5 μL of the suspension (1.0 mg mL^{-1}) was dropped to the electrode surface and dried in air.

Similarly, Lac/RGO–Pd NPs/GCE, Lac/RGO–Cu NPs/GCE, and Lac/RGO/GCE were fabricated by replacing RGO–PdCu NCs with RGO–Pd NPs, RGO–Cu NPs, or RGO, while the other experimental conditions were kept the same. All the electrodes were stored in refrigerator when not in use.

To examine the bioelectrocatalytic activity of the immobilized Lac towards catechol oxidation, cyclic voltammetry and chronoamperometry measurements were performed in 0.2 M acetate buffer solutions by previously bubbling with highly purified nitrogen gas for 30 min. All the experiments were performed at room temperature, if not stated otherwise.

3. Results and discussion

3.1. Characterization

As displayed by TEM images (Fig. 1A and B), the typical product contains a large numbers of well-defined particles with pinholes formed on walls, edges, and corners, indicating the formation of nanocages with an average diameter of 58.8 nm (inset in Fig. 1A), which are uniformly deposited on the surfaces of reduced graphene oxide (RGO) as marked by the arrows. The detailed morphology and hollow structures are further elucidated by individual nanocage (Fig. 1C). It can be seen that the nanostructures have clear edges, corners and porous structures. Also, their polycrystalline nature is strongly demonstrated by the SAED pattern (inset in Fig. 1B) (Lv et al., 2014a, 2014b, 2014c). In addition, the only existence of $Pd(acac)_2$ as the precursor induces the formation of irregular nanoparticles (Fig. S1A, Electronic Supplementary Material, ESM) while nanocluster products are obtained in the case of $Cu(acac)_2$ as the precursor (Fig. S1B, ESM).

HR-TEM images provide more detailed information of the sample (Fig. 1E and F), in which clear lattice fringes are observed with the interplanar distance of 0.211 nm corresponding to the (111) crystal planes of the face-centered cubic (fcc) PdCu alloy (Mao et al., 2014). This value coincidentally locates between the (110) crystal planes of bulk Pd (0.246 nm, JCPDS no. 46-1043) and Cu (0.209 nm, JCPDS no. 04-0836), reflecting the formation of PdCu alloy. This observation is similar to the previous study in the literature (Wang et al., 2013).

The HADDF-STEM-EDS elemental mapping images (Fig. 2A–C) and cross-section compositional line profiles (Fig. 2D) were recorded to analyze the distribution of Pd and Cu in PdCu NCs. It can be seen that Pd and Cu elements are homogeneously distributed throughout an entire nanocage, which shows the formation of PdCu alloy (Zhang et al., 2011), as demonstrated by the HR-TEM analysis.

As illustrated in Fig. S2 (ESM), XRD analysis was conducted to characterize the crystalline phase structure of RGO–PdCu NCs (curve a). There are four typical diffraction peaks emerged at 41.6°, 48.3°, 72.5°, and 86.9°, which are well assigned to the (111), (200), (220), and (311) crystal planes of the fcc PdCu alloy (Lv et al., 2014a, 2014b, 2014c). These diffraction peaks are coincidentally

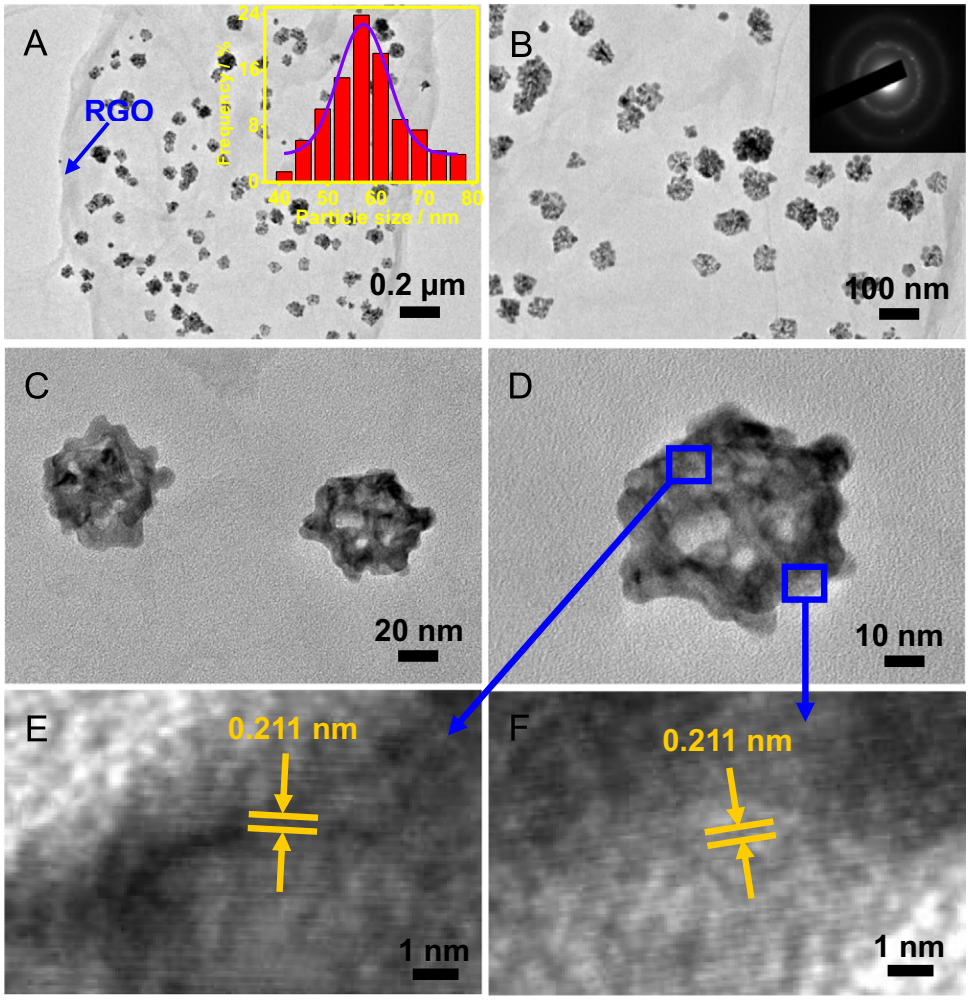

Fig. 1. (A–D) TEM and (E–F) HR-TEM images of RGO–PdCu NCs. Inset in B shows the corresponding SAED pattern.

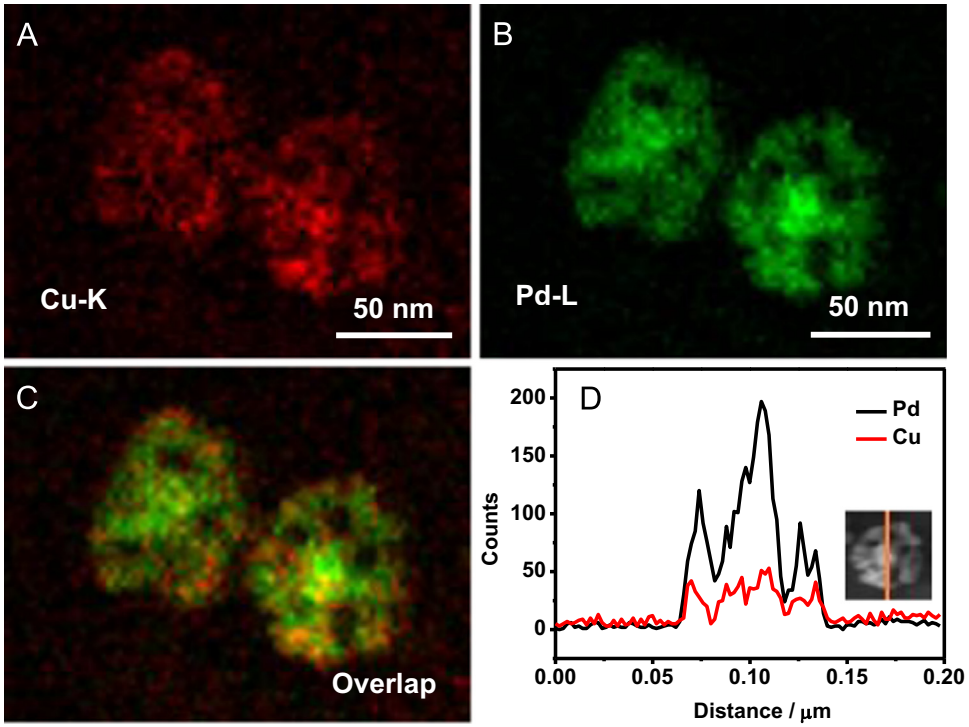

Fig. 2. (A–C) HAADF-STEM-EDS mapping images and (D) line scanning profiles of RGO–PdCu NCs.

situated between bulk Pd (JCPDS no. 46-1043) and Cu (JCPDS no. 04-0836), strongly showing the formation of Pd–Cu alloy (Yin et al., 2012). These observations are matched well with those in the previous literature (Gao et al., 2003). Additionally, a broad diffraction peak at 19.9° is detected for RGO–PdCu NCs, which is different from that of blank GO ($2\theta = 10.8°$, curve b, Fig. S2, ESM), indicating the efficient reduction of GO to RGO (Sahoo et al., 2014).

XPS measurements were performed to further characterize the surface states and compositions of RGO–PdCu NCs (Fig. S3A, ESM). The survey XPS spectrum reveals that the diffraction peaks located at 976.8, 531.7, 345.0, and 285.5 eV are well assigned to Cu, O, Pd, and C elements, respectively. These observations are strongly supported by the corresponding EDS spectra (Fig. S4, ESM).

As described by the high-resolution C 1s XPS spectra (Fig. S3B, ESM), the peak at 285.5 eV can be further divided into three peaks at 284.2, 285.9, and 289.4 eV, which are assigned to the C–C (sp^2 C), C–O, and C=O groups, respectively (Fan et al., 2010). Interestingly, the intensity of the sp^2 C–C peak is much stronger than the others, indicating the efficient reduction of GO to RGO in the present synthesis (Lv et al., 2014a, 2014b, 2014c).

For the high-resolution Cu 2p XPS spectrum (Fig. S3C, ESM), Cu 2p peak can be deconvoluted into two strong peaks at 932.3 and 950.5 eV, which are assigned to the binding energies of Cu $2p_{3/2}$ and Cu $2p_{1/2}$ of metallic Cu (0) (Brege et al., 2009), respectively. There is no distinct peak of Cu^{2+} emerged at 942 eV, revealing that metallic Cu (0) is the predominant species in PdCu NCs (Jia et al., 2013). Besides, similar trend is observed from the Pd 3d XPS spectrum (Fig. S3D, ESM), manifesting the predominant existence of metallic Pd (0) in PdCu NCs (Vadahanambi et al., 2011). The above results demonstrate the efficient reduction of GO and the precursors ($Pd(acac)_2$ and $Cu(acac)_2$) after the solvothermal process (Lv et al., 2014a, 2014b, 2014c).

Raman spectroscopy is a powerful tool to characterize graphene-based nanomaterials (Fig. S5A, ESM). There are two characteristic peaks emerged at 1330 and 1596 cm^{-1} for RGO–PdCu NCs (curve a), corresponding to the *D* and *G* bands (Li et al., 2014a, 2014b, 2014c), respectively. The former is associated with the A_{1g} breathing mode of disordered structures of graphite, while the latter is correlated with the doubly degenerate E_{2g} of graphite (Zhao et al., 2012). It is noticed that the two bands are broadened and blue shifted in comparison with those of GO (curve b) under the same conditions. Meanwhile, the intensity ratio of the *D* to *G* bands (denote as I_D/I_G) is 1.12 for RGO–PdCu NCs, which is larger than that of GO (0.68). This ratio is similar to that of Pt–Pd NFs/RGOs (1.10) in the literature (Lv et al., 2014a, 2014b, 2015c). These results manifest the formation of smaller in-plane sp^2 domains after the reduction of GO and again verify the formation of RGO (Lv et al., 2014a, 2014b, 2014c).

The thermal stability of RGO–PdCu NCs (curve a) was examined by TGA measurements (Fig. S5B, ESM), using GO (curve b) as a reference. The weight loss of RGO–PdCu NCs under 100 °C is assigned to water evaporation (Stankovich et al., 2007), while those in the range of 350–540 °C and 630–720 °C are assigned to the pyrolysis of oxygenated functional groups, and combustion of carbon skeleton of RGO (Zhao et al., 2012), respectively. This trend is much slower for RGO–PdCu NCs as compared to that of GO under the identical conditions. These results manifest the improved thermal stability of RGO–PdCu NCs. Additionally, the mass loading of PdCu NCs is 56.5 wt% for RGO–PdCu NCs.

Electrochemical impedance spectroscopy (EIS) experiments were conducted to monitor the construction procedure of Lac/RGO–PdCu NCs/GCE, which is effective to probe the changes on the electrode surface (Gao et al., 2011; Wang et al., 2014). As shown in Fig. S6 (ESM), the impedance features are presented by Nyquist plots at different modification steps, in which significant changes are observed during the process. After the modification with RGO–PdCu NCs, the diameter of semicircle (curve b) is increased as compared to that of bare GCE (curve a), implying that RGO–PdCu NCs obstruct the electron transfer of the redox-probe ($[Fe(CN)_6]^{3-/4-}$), which confirm the effective deposition of RGO–PdCu NCs on the electrode surface. After the immobilization of Lac molecules onto RGO–PdCu NCs, the diameter of the semicircle (curve c) is significantly increased, demonstrating the efficient immobilization of Lac molecules on RGO–PdCu NCs/GCE.

3.2. Optimization of the operating conditions

Catechol is an important intermediate in many biological and environmental processes, and thus its accurate determination has great practical values (Su et al., 2011). The pH influence was investigated through the catalytic responses of Lac/RGO–PdCu/GCE toward 1.0 mM catechol in the pH range between 4.0 and 7.0. As shown in Fig. S7A (ESM), the catalytic currents of Lac/RGO–PdCu/GCE increase with the pH values from 4.0 and reach the maximum at pH 5.0. Further increasing the pH values adversely induces the decrease of the catalytic currents. Therefore, pH 5.0 was chosen as the optimal pH value in 0.2 M acetate buffer.

Meanwhile, the variation of the applied potentials from 0.3 to 0.7 V also brought great changes of the catalytic currents at Lac/RGO–PdCu/GCE, while other experimental conditions were kept the same (Fig. S7B, ESM). The catalytic currents achieve the maximum at 0.6 V, and then drop down by further increasing the applied potentials. As a result, 0.6 V was selected as the optimal applied potential in the following experiments.

3.3. Electrocatalytic activity toward the oxidation of catechol

The electrocatalytic activity of Lac/RGO–PdCu NCs/GCE (curve a) were examined, using Lac/RGO–Pd NPs/GCE (curve b), Lac/RGO–Cu NPs/GCE (curve c), Lac/RGO/GCE (curve d), and bare GCE (curve e) as referenced electrodes (Fig. S8, ESM). It is observed that all the electrodes show a pair of redox peaks in 0.2 M acetate buffer solution (pH 5.0). Clearly, the highest oxidation peak current is found at Lac/RGO–PdCu NCs/GCE for catechol oxidation as compared to RGO–Pd NPs/GCE, Lac/RGO–Cu NPs/GCE, and Lac/RGO/GCE, reflecting the significantly enhanced electrocatalytic activity of Lac/RGO–PdCu NCs.

The enhanced responses of Lac/RGO–PdCu NCs/GCE are attributed to the following factor: (1) the d-band center shifted upwards towards the Fermi level for Pd–Cu bimetallic nanostructure as compared to the parent Pd, resulting in the increase in the adsorbate-binding energy (Hammer and Nørskov, 2000). (2) The flexible RGO sheets form an effective matrix to enwrap PdCu NCs that can effectively prevent their detachment and agglomeration during cycling (Hu et al., 2014).

Fig. 3 illustrates the sensing mechanism for laccase

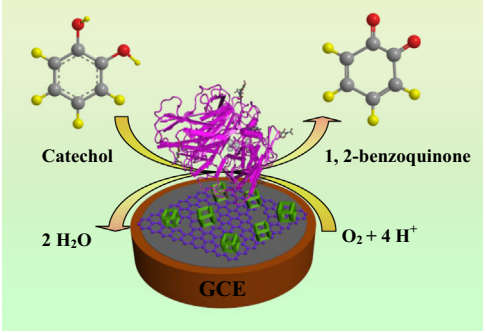

Fig. 3. Schematic illustration of the catalyzed oxidation of catechol by laccase on the electrode surface.

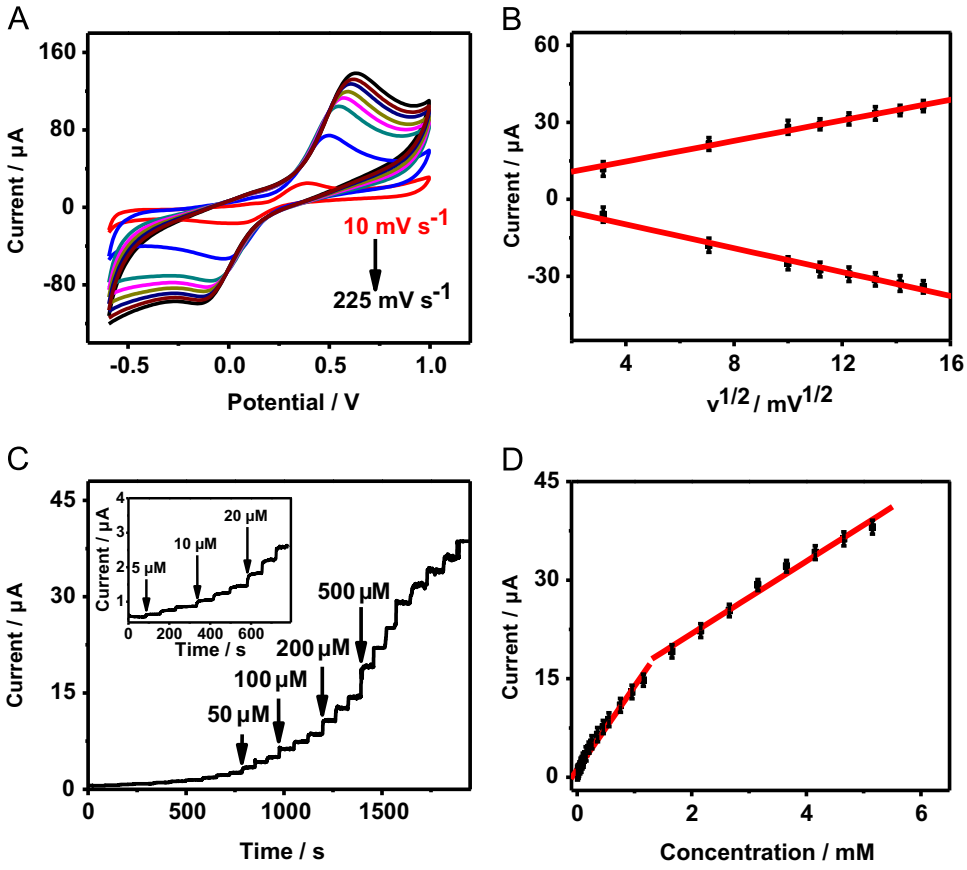

Fig. 4. (A) CVs of Lac/RGO–PdCu NCs/GCE in 0.2 M acetate buffer solution (pH 5.0) containing 1.0 mM catechol at different scan rates: 10, 50, 100, 125, 150, 175, 200, and 225 mV s^{-1}. (B) The plot of the peak currents against the scan rates. (C) Amperometric responses of Lac/RGO–PdCu NCs/GCE after successive addition of catechol. (D) The calibration curves of the catalytic currents *vs.* catechol concentrations. The error bars indicate the standard error for five measurements with the same electrode.

electrocatalyzing catechol oxidation with the underlying electrode. In this process, catechol is oxidized to its corresponding 1, 2-benzoquinone upon in contact with Lac, coupled with the electrocatalytic reduction of dioxygen to water on the electrode surface. The resulting oxidation current is quantitatively proportional to the concentration of phenolic compound.

Laccase has the ability to catalyze the oxidation of many hydroxylation reactions of monophenols, diphenols, and aromatic amine (Zhou et al., 2014). The catalyzed reaction processes are described as follows:

$$\text{Catechol} + \text{Laccase(oxy)} \rightarrow \text{1, 2–Benzoquinone} + \text{Laccase(deoxy)} + 2H^+ + 2e^- \quad (1)$$

$$\text{Laccase(deoxy)} + O_2 + 4H^+ \rightarrow \text{Laccase(oxy)} + 2H_2O \quad (2)$$

The cyclic voltammograms (CVs) of Lac/RGO–PdCu NCs/GCE were recorded in 0.2 M acetate buffer solution (pH 5.0) containing 1.0 mM catechol at different scan rates (Fig. 4A). The oxidation and reduction peak currents of catechol enhance with the scan rates, and are proportional to the square roots of the scan rates (Fig. 4B). It means that the electrochemical reaction here is a diffusion-controlled electron-transfer process at Lac/RGO–PdCu NCs/GCE (Zhang et al., 2014).

As illustrated in Fig. 4C, the catalytic responses of Lac/RGO–PdCu NCs/GCE for catechol are fast (less than 3s) under the optimized experimental conditions, and linearly increase with catechol concentrations. Fig. 4D shows the corresponding calibration plot of the catalytic currents *vs.* catechol concentrations. There are two linear ranges: the former is located between 0.005 and 1.155 mM with the sensitivity of 12.65 μA mM^{-1} and the detection limit of 1.5 μM at a signal-to-noise ratio of 3 ($S/N=3$, linear regression equations: I (μA)$=1.19+12.65C_{catechol}$, $R^2=0.9835$), while the later appears from 1.655 to 5.155 mM with the sensitivity of 5.51 μA mM^{-1} and the detection limit is estimated to be 2.0 μM at $S/N=3$ (linear regression equations: I (μA)$=10.84+5.51C_{catechol}$, $R^2=0.9851$). As shown in Table S1 (ESM), the resulting Lac/RGO–PdCu NCs/GCE displays comparable or even better catalytic activity for catechol determination as relative to those in the literature (Fu et al., 2014; Shimomura et al., 2011; Zhou et al., 2013, 2014).

Furthermore, the reproducibility and repeatability of Lac/RGO–PdCu NCs/GCE were also investigated. The electrode-to-electrode reproducibility was evaluated from the response to 1.0 mM catechol at five different sensors prepared independently (Fig. S9A, ESM). The relative standard deviation (RSD) was 4.1%. The repeatability of the same electrode was examined by five successive measurements under the same conditions with the RSD of 3.1%, indicating good repeatability of Lac/RGO–PdCu NCs/GCE without any pretreatment involved. After the storage of 35 days at 4 °C, the catalytic currents still remained 98.90% of its original values on Lac/RGO–PdCu NCs/GCE (Fig. S9B, ESM). These results strongly evidence good reproducibility and stability of Lac/RGO–PdCu NCs/GCE, owing to the strong interactions between enzyme and the modified electrode (Gao et al., 2014).

3.4. Application to real sample analysis

To further confirm the suitability and potential application for sample analysis, this biosensor was used to detect catechol in tea samples. After these tea samples were immersed in 100 mL water for 24 h, 0.027 mg g^{-1} of catechol were detected by the Lac/RGO–

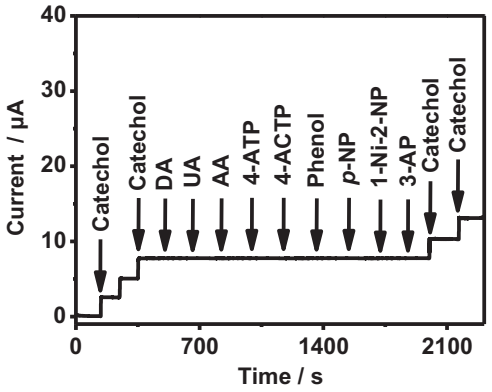

Fig. 5. Amperometric responses of Lac/RGO–PdCu NCs/GCE after the addition of different interfering substances.

PdCu NCs/GCE biosensor. As illustrated in Table S2 (ESM), the recoveries of catechol standard solutions added into the samples were in the range of 98.80–102.19% for three independent measurements, with relative standard deviations (RSD) less than 3.7%. It means that the as-developed phenol biosensor can be applied to the detection of phenol compounds in real samples even crowed with many undefined substances.

Another important issue for a biosensor is the capability to distinguish the target molecules from the interferences commonly presented in acid media (Li et al., 2014a, 2014b, 2014c). Fig. 5 shows the catalytic currents of Lac/RGO–PdCu NCs/GCE towards different chemicals with the same concentrations (0.5 M), including uric acid (UA), dopamine (DA), ascorbic acid (AA), 4-aminothiophenol (4-ATP), 4-acetaminophenol (4-ACTP), phenol, *p*-nitrophenol (*p*-NP), 1-nitroso-2-naphthol (1-Ni-2-NP), 3-aminophenol (3-AP), 500 folds of Ca^{2+}, Mg^{2+}, K^{+}, and Na^{+}, and 50 folds of lactic acid and glutaric acid. These interferences display no obvious interference to catechol detection, indicating the improved selectivity of the obtained biosensor.

4. Conclusions

In summary, well-defined RGO–PdCu NCs were facilely prepared by a simple one-pot solvothermal method. A novel phenol biosensor was constructed based on RGO–PdCu NCs and laccase. The resulting biosensor displayed improved catalytic performances toward catechol oxidation compared with referenced biosensors, as well as many other advantages such as high selectivity, low detection limit, good reproducibility and stability. This biosensor was further explored for rapid detection of catechol in tea samples, which would be a good candidate for the applications of a highly sensitive phenolic biosensor.

Acknowledgment

This work was financially supported by National Natural Science Foundation of China (Nos. 21475118, 21175118, 21275130 and 21275131).

Appendix A. Supplementary material

Supplementary data associated with this article can be found in the online version at http://dx.doi.org/10.1016/j.bios.2015.06.060.

References

Barek, J., Ebertova, H., Mejstrík, V., Zima, J., 1994. Collect. Czechoslov. Chem. Commun. 59, 1761–1771.
Brege, J.J., Hamilton, C.E., Crouse, C.A., Barron, A.R., 2009. Nano Lett. 9, 2239–2242.
Brondani, D., de Souza, B., Souza, B.S., Neves, A., Vieira, I.C., 2013. Biosens. Bioelectron. 42, 242–247.
Fan, Z., Wang, K., Wei, T., Yan, J., Song, L., Shao, B., 2010. Carbon 48, 1686–1689.
Fu, J., Qiao, H., Li, D., Luo, L., Chen, K., Wei, Q., 2014. Sensors 14, 3543–3556.
Gao, H., Xiao, F., Ching, C.B., Duan, H., 2011. ACS Appl. Mater. Interfaces 3, 3049–3057.
Gao, W., Guan, N., Chen, J., Guan, X., Jin, R., Zeng, H., Liu, Z., Zhang, F., 2003. Appl. Catal. B 46, 341–351.
Gao, Y.-F., Yang, T., Yang, X.-L., Zhang, Y.-S., Xiao, B.-L., Hong, J., Sheibani, N., Ghourchian, H., Hong, T., Moosavi-Movahedi, A.A., 2014. Biosens. Bioelectron. 60, 30–34.
Giardina, P., Faraco, V., Pezzella, C., Piscitelli, A., Vanhulle, S., Sannia, G., 2010. Cell. Mol. Life Sci. 67, 369–385.
Hammer, B., Nørskov, J.K., 2000. Adv. Catal. 45, 71–129.
Hu, C., Zhai, X., Zhao, Y., Bian, K., Zhang, J., Qu, L., Zhang, H., Luo, H., 2014. Nanoscale 6, 2768–2775.
Hummers Jr., W.S., Offeman, R.E., 1958. J. Am. Chem. Soc. 80, 1339.
Jia, X., Li, J., Wang, E., 2013. Small 9, 3873–3879.
Lee, K., Mazare, A., Schmuki, P., 2014. Chem. Rev. 114, 9385–9454.
Li, D., Liu, J., Barrow, C.J., Yang, W., 2014. Chem. Commun. 50, 8197–8200.
Li, D., Luo, L., Pang, Z., Ding, L., Wang, Q., Ke, H., Huang, F., Wei, Q., 2014. ACS Appl. Mater. Interfaces 6, 5144–5151.
Li, S.-S., Lv, J.-J., Hu, Y.-Y., Zheng, J.-N., Chen, J.-R., Wang, A.-J., Feng, J.-J., 2014. J. Power Sources 247, 213–218.
Lv, J.-J., Li, S.-S., Wang, A.-J., Mei, L.-P., Chen, J.-R., Feng, J.-J., 2014. Electrochim. Acta 136, 521–528.
Lv, J.-J., Li, S.-S., Wang, A.-J., Mei, L.-P., Feng, J.-J., Chen, J.-R., Chen, Z., 2014. J. Power Sources 269, 104–110.
Lv, J.-J., Zheng, J.-N., Zhang, H.-B., Lin, M., Wang, A.-J., Chen, J.-R., Feng, J.-J., 2014. J. Power Sources 269, 136–143.
Mao, J., Liu, Y., Chen, Z., Wang, D., Li, Y., 2014. Chem. Commun. 50, 4588–4591.
Marrubini, G., Calleri, E., Coccini, T., Castoldi, A., Manzo, L., 2005. Chromatographia 62, 25–31.
Naczk, M., Shahidi, F., 2004. J. Chromatogr. A 1054, 95–111.
Niu, X., Chen, C., Zhao, H., Chai, Y., Lan, M., 2012. Biosens. Bioelectron. 36, 262–266.
Portaccio, M., Di Tuoro, D., Arduini, F., Lepore, M., Mita, D., Diano, N., Mita, L., Moscone, D., 2010. Biosens. Bioelectron. 25, 2003–2008.
Sahoo, P.K., Panigrahy, B., Bahadur, D., 2014. RSC Adv. 4, 48563–48571.
Sahu, S.C., Samantara, A.K., Satpati, B., Bhattacharjee, S., Jena, B.K., 2013. Nanoscale 5, 11265–11274.
Shimomura, T., Itoh, T., Sumiya, T., Hanaoka, T.-A., Mizukami, F., Ono, M., 2011. Sens. Actuators B: Chem. 153, 361–368.
Skladal, P., Morozova, N.O., Reshetilov, A.N., 2002. Biosens. Bioelectron. 17, 867–873.
Stankovich, S., Dikin, D.A., Piner, R.D., Kohlhaas, K.A., Kleinhammes, A., Jia, Y., Wu, Y., Nguyen, S.T., Ruoff, R.S., 2007. Carbon 45, 1558–1565.
Stoytcheva, M., Zlatev, R., Triny Beleno, M., Montero, G., 2015. Curr. Anal. Chem. 11, 50–55.
Su, J., Chen, F., Cryns, V.L., Messersmith, P.B., 2011. J. Am. Chem. Soc. 133, 11850–11853.
Tan, Y., Deng, W., Ge, B., Xie, Q., Huang, J., Yao, S., 2009. Biosens. Bioelectron. 24, 2225–2231.
Vadahanambi, S., Jung, J.-H., Oh, I.-K., 2011. Carbon 49, 4449–4457.
Wang, L., Lu, X., Wen, C., Xie, Y., Miao, L., Chen, S., Li, H., Li, P., Song, Y., 2015. J. Mater. Chem. A 3, 608–616.
Wang, L., Zhang, Q., Chen, S., Xu, F., Chen, S., Jia, J., Tan, H., Hou, H., Song, Y., 2014. Anal. Chem. 86, 1414–1421.
Wang, M., Zhang, W., Wang, J., Minett, A., Lo, V., Liu, H., Chen, J., 2013. J. Mater. Chem. A 1, 2391–2394.
Wightman, R.M., 2006. Science 311, 1570–1574.
Wolfrum, B., Zevenbergen, M., Lemay, S., 2008. Anal. Chem. 80, 972–977.
Yang, F., Yang, Z., Zhuo, Y., Chai, Y., Yuan, R., 2015. Biosens. Bioelectron. 66, 356–362.
Yin, Z., Zhou, W., Gao, Y., Ma, D., Kiely, C.J., Bao, X., 2012. Chem. Eur. J. 18, 4887–4893.
Zhang, H., Jin, M., Liu, H., Wang, J., Kim, M.J., Yang, D., Xie, Z., Liu, J., Xia, Y., 2011. ACS Nano 5, 8212–8222.
Zhang, Y., Li, Y., Wu, W., Jiang, Y., Hu, B., 2014. Biosens. Bioelectron. 60, 271–276.
Zhao, L., Li, S., He, J., Tian, G., Wei, Q., Li, H., 2013. Biosens. Bioelectron. 49, 222–225.
Zhao, Y., Song, X., Song, Q., Yin, Z., 2012. CrystEngComm 14, 6710–6719.
Zhou, X.-H., Liu, L.-H., Bai, X., Shi, H.-C., 2013. Sens. Actuators B: Chem. 181, 661–667.
Zhou, Y., Tang, L., Zeng, G., Chen, J., Cai, Y., Zhang, Y., Yang, G., Liu, Y., Zhang, C., Tang, W., 2014. Biosens. Bioelectron. 61, 519–525.